

**First-principles-based embedded atom method for PdAu nanoparticles**Bin Shan,<sup>1,\*</sup> Ligen Wang,<sup>1</sup> Sang Yang,<sup>1</sup> Jangsuk Hyun,<sup>1</sup> Neeti Kapur,<sup>1</sup> Yujun Zhao,<sup>1</sup> John B. Nicholas,<sup>1</sup> and Kyeongjae Cho<sup>2,†</sup>  
<sup>1</sup>*Nanostellar Inc., Redwood City, California 94063, USA*<sup>2</sup>*Department of Materials Science and Engineering and Department of Physics, University of Texas at Dallas, Richardson, Texas 75080, USA*

(Received 2 March 2009; revised manuscript received 15 June 2009; published 8 July 2009)

One of the key problems in studying alloy nanoparticle catalysis is their surface morphology and segregation behavior. We have developed an accurate embedded atom method (EAM) potential and employed it in the simulation of PdAu metal alloy nanoparticles. The potential was parameterized based on an extensive set of density-functional-theory (DFT) calculations of metal clusters in addition to bulk-alloy properties. The EAM potential accurately reproduces DFT energies of both bulk PdAu alloys and small nanoparticles. We utilized the developed EAM potential in a Monte Carlo simulation of PdAu nanoparticles ranging from 55-atom ( $\sim 1$  nm) to 5083-atom particles ( $\sim 4.5$  nm). The effects of different factors (particle size, temperature, and composition ratios) on the segregation behavior of PdAu alloy are examined. Our simulation results quantitatively reveal the extent of surface segregation and a strong dependence of surface morphology on the nanoparticle size.

DOI: [10.1103/PhysRevB.80.035404](https://doi.org/10.1103/PhysRevB.80.035404)

PACS number(s): 71.15.-m, 31.15.A-, 81.16.Hc

**I. INTRODUCTION**

Bimetallic nanoparticles (NPs) have been widely used in applications such as electrochemistry and surface catalysis. Large surface areas and properties due to quantum-confinement effects have attracted great interest in the nanoparticle research community. Bimetallic nanoparticles enable additional engineering flexibility in reactivity control through doping or alloying. Higher activity of bimetallic systems can be achieved via bifunctional mechanism,<sup>1</sup> electronic effects,<sup>2,3</sup> or geometric ensemble effects.<sup>4,5</sup> Recently, it has been shown that PdAu bimetallic nanoparticle catalysts exhibit good stability and excellent reactivity toward a number of chemical reactions, such as aromatics hydrogenation,<sup>6</sup> CO oxidation,<sup>4,7</sup> and vinyl acetate synthesis.<sup>5</sup> Furthermore, it has been demonstrated experimentally that ensemble patterns (e.g., Pd atom cluster on surface) play a key role in the catalytic reactivity of bimetallic surfaces.<sup>4,5,8</sup> Therefore, a detailed atomistic understanding of nanoparticle surface morphology will greatly benefit the design and optimization of alloy nanoparticle catalysts.

Over the years, density-functional-theory (DFT) calculations have been extensively used to study the electronic and catalytic properties of alloy nanoparticles. Such approach has led to considerable progress in the fundamental understanding of nanoparticle catalysis.<sup>3,9-11</sup> However, in practical catalyst systems, the average number of atoms in a catalyst particle usually goes well beyond a thousand, making direct first-principles DFT calculations prohibitively expensive.<sup>12</sup> To overcome the size limitation of DFT method and to apply atomistic simulations of segregation, defects, diffusion to systems with large number of atoms, many empirical methods have been developed by approximating the fast moving electrons as an “effective medium” and only dealing with the slower movement of the ions.<sup>13-17</sup> This provides a highly efficient method of calculating the energetic and structural properties of atomistic systems. The embedded atom method (EAM) is the most common and successful model in describ-

ing atomic bonding in metallic systems.<sup>13,14,18</sup> However, when applied to metallic nanoparticles, EAM potentials that are parameterized to bulk material properties generally do not reproduce accurate binding energies since metal atoms in nanoparticles experience different local environment. Recently, some efforts toward predicting a more accurate binding energy for nanoparticles have been made by including additional parameters to reflect the local asymmetric charge distribution.<sup>19</sup>

In this paper, we report an extension of EAM potentials to small nanoparticles and specifically address PdAu alloy systems. This is made possible by refining the original EAM embedding and cross-pair functionals, as well as incorporating additional geometric and energetic properties of nanoparticles from first-principles calculations into parameterization. Data sets that are used for EAM parameterization include bulk material properties, slab energies, and cluster energies (from dimers to 147-atom cluster), all calculated within DFT framework and at the Perdew-Burke-Erzerhof (PBE) functional level.<sup>20</sup> The parameterized EAM potentials of the metals and alloys reproduce faithfully energies of nanoparticles down to several atoms in size. The parameterized Pd-Au cross-pair potential also agrees well with alloy heats of formation for PdAu alloy nanoparticles. As an example of the utilization of the developed EAM potential, we carried out Monte Carlo (MC) simulations of PdAu alloy nanoparticles ranging from 55-atom ( $\sim 1$  nm) to 5083-atom ( $\sim 4.5$  nm). We demonstrate how factors such as temperature, particle size, and the alloy composition ratio influence surface concentration of the constituent metals. The statistical analysis of monomer and dimer distribution on different metal facets shows how catalytically active sites change under different conditions. The availability of a highly accurate EAM alloy potential would facilitate a better understanding of alloy nanoparticle properties and their application in catalysis.

**II. THEORETICAL METHODS**

We briefly describe in the following sections the procedures we have used in the DFT calculations, EAM param-

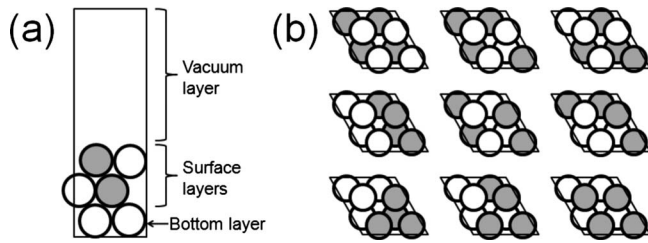


FIG. 1. (a) Side view of the unit cell (b) Top view of different configurations of  $\text{Pd}_4\text{Au}_4$  in the surface layers. White circles represent Pd atoms and gray circles represent Au atoms.

eterization for pure elements and alloys, and the MC simulations of different sized PdAu nanoparticles.

### A. Density functional theory

Self-consistent DFT calculations was carried out with Perdew-Burke-Ernzerhof (generalized gradient approximation of the exchange-correlation functional, which has been shown to give accurate results for a variety of molecular energies and structures.<sup>20</sup> The VIENNA AB INITIO SIMULATION PACKAGE (VASP) was used for the calculations.<sup>21</sup> The Kohn-Sham single-electron wave function was expanded by plane waves with an energy cutoff of 400 eV, which is tested to give good convergence for total system energies. The geometry optimization was terminated when the Hellmann-Feynman force on each atom was less than  $0.05 \text{ eV}/\text{\AA}$ .

A  $9 \times 9 \times 9$   $k$ -point mesh was used to sample the first Brillouin zone of bulk palladium and gold. The DFT optimized lattice constants for Pd and Au were 3.95 and 4.18  $\text{\AA}$ , in good agreement with experimental values of 3.89 and 4.08  $\text{\AA}$ .<sup>22</sup> The total-energy curves for unit-cell distortions corresponding to elastic constants ( $C_{11}, C_{12}, C_{44}$ ) were calculated by employing suitable lattice distortions of the unit cell.<sup>23</sup> The heats for formation of PdAu alloy were calculated assuming  $L_{10}$  intermetallic structure for 1:1 composition ratio and  $L_{12}$  intermetallic structure for 1:3 and 3:1 composition ratio PdAu alloy, respectively.

For PdAu alloy surface properties we have used a  $p(2 \times 2)$  surface cell with four metal atoms per layer. The metal slab consists of three layers, with pure Pd atoms as the bottom layer fixed at their crystallographic bulk lattice positions, and the rest of the atoms free to relax in all directions. After excluding geometries related by symmetry, a total of 33 unique configurations with different composition ratios of Pd and Au for the first two layers were considered. An example of all nine possible configurations with four Pd atoms and four Au atoms in the first two surface layers is shown in Fig. 1. A  $4 \times 4 \times 1$   $k$ -point mesh was used and a vacuum layer of 11  $\text{\AA}$  was introduced to separate the slab images in the  $z$  direction.

Beside the bulk and surface properties, we have also calculated the energies of a series of nanoparticles to be included in the parameterization of the EAM potential. These nanoparticles have metal atoms sitting on vertex and edge sites that have significantly lower electron density than that in a bulk site. For pure metals, we have calculated the energies of clusters ranging from dimer to 147-atom cluster (Fig.

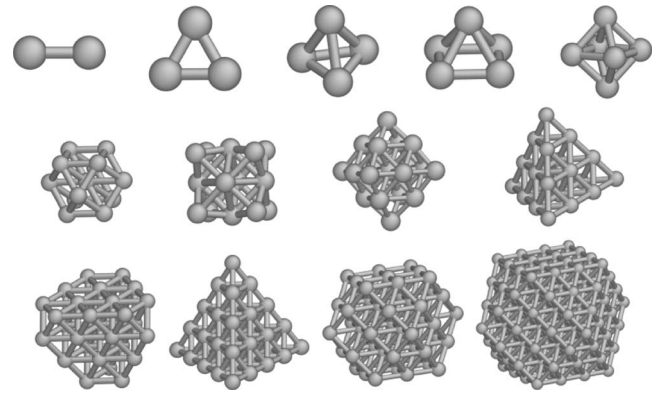


FIG. 2. Geometries of metal clusters included in the parameterization of EAM potential. They are  $M_2, M_3, M_4, M_5, M_6, M_{13}, M_{14}, M_{19}, M_{20}, M_{31}, M_{35}, M_{55}$ , and  $M_{147}$ , respectively.

2). The binding energy per atom for pure cluster is defined as  $\Delta E_{\text{binding}} = (\Delta E_{\text{total}} - N \cdot \Delta E_{\text{atom}}) / N$ , where  $N$  is the number of total atoms in the cluster. For PdAu alloy nanoparticles, we calculated the energies of a  $\text{Pd}_{43}\text{Au}_{12}$  icosahedral nanoparticle with different number of Au atoms on the surface and in different positions. A total of nine configurations are considered ranging from all Au atoms segregated on the surface to all Au atoms in the interior of the nanoparticle as shown in Fig. 3. All nanoparticle calculations are done with a  $1 \times 1 \times 1$   $k$ -point mesh and a supercell of  $24 \times 24 \times 24 \text{ \AA}$  to avoid image interactions.

### B. Embedded atom method for nanoparticles

Embedded Atom Method is a local environment-dependent interatomic potential, that is, particularly effective in describing metallic systems.<sup>13,14,18,24,25</sup> The coarse graining of valence electrons to interatomic bonding also makes it computationally efficient to handle systems with large number of atoms, such as film growth<sup>24,25</sup> or nanoparticle segregation.<sup>26,27</sup> The EAM total energy of an  $N$ -atom system can be expressed as a sum of embedding energy and a pairwise interaction energy,

$$E_{\text{tot}}[R_1, \dots, R_N] = \sum_i F[\rho_i] + \sum_{i < j} \phi[R_{ij}], \quad (1)$$

where  $R_1, \dots, R_N$  denote the atomic coordinates of  $N$  atoms in the system and  $F$  is the embedding function representing

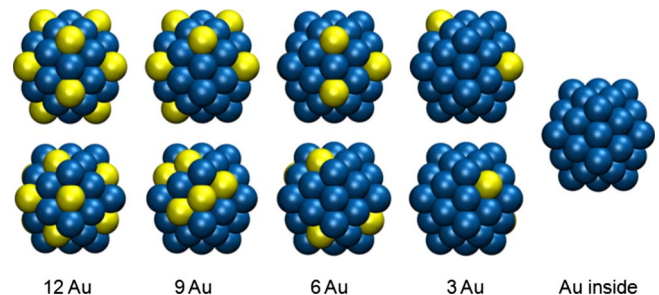


FIG. 3. (Color online) Geometries for  $\text{Pd}_{43}\text{Au}_{12}$  nanoparticles as a function of surface Au concentration. Text below each column indicates the number of Au atoms available on the nanoparticle surface.

the energy of embedding an atom in a host electron density  $\rho$ .  $\phi$  represents the pairwise interactions between neighboring atoms located at  $R_i$  and  $R_j$ . The host electron density  $\rho_i$  is a summation of the spherically symmetric electron-density contributions from neighboring atoms  $\rho_i = \sum_{j \neq i} \rho_j [R_{ij}]$ . The most common way of devising the embedding function and pair potentials is to fit some physically reasonable functional forms to materials properties such as lattice constant and cohesive energies. Many proposed functional forms for em-

bedding energies and pairwise interactions work reasonably accurately for predicting the total energy of bulk systems.<sup>16,28–30</sup> We adopted Zhou's parameterization scheme with slight modifications for our EAM potential scheme.<sup>24,29</sup> An additional spline function is added for the embedding function in the low electron-density region from  $\rho_m$  to  $\rho_n$  to capture the low electron-density environments in nanoparticles. The explicit functional forms for  $F(\rho_i)$ ,  $\phi(R_{ij})$ , and  $\rho_i$  are given in Eqs. (2)–(4), respectively.

$$F(\rho_i) = \begin{cases} \sum_{i=0}^3 F_{mi} \left( \frac{\rho_i}{\rho_m} - 1 \right)^i, & 0 \leq \rho_i < \rho_m, \\ \sum_{i=0}^3 F_{ni} \left( \frac{\rho_i}{\rho_n} - 1 \right)^i, & \rho_m \leq \rho_i < \rho_n, \quad \rho_n = 0.85\rho_e, \\ \sum_{i=0}^3 F_i \left( \frac{\rho_i}{\rho_e} - 1 \right)^i, & \rho_n \leq \rho_i < \rho_0, \quad \rho_0 = 1.15\rho_e, \\ F_e \left[ 1 - \ln \left( \frac{\rho_i}{\rho_s} \right)^\eta \right] \left( \frac{\rho_i}{\rho_s} \right)^\eta, & \rho_i > \rho_0, \end{cases} \quad (2)$$

$$\phi(R_{ij}) = \frac{A \exp[-\alpha(R_{ij}/r_e - 1)]}{1 + (R_{ij}/r_e - \kappa)^{20}} - \frac{B \exp[-\beta(R_{ij}/r_e - 1)]}{1 + (R_{ij}/r_e - \lambda)^{20}}, \quad (3)$$

$$\rho_i = \sum_{j \neq i} \left\| \frac{f_e \exp[-\beta(R_{ij}/r_e - 1)]}{1 + (R_{ij}/r_e - \lambda)^{20}} \right\|. \quad (4)$$

The embedding function  $F(\rho_i)$  has the form of cubic equations. Adjustable parameters,  $F_{mi}$ ,  $F_{ni}$ ,  $F_i$ ,  $F_e$ , and  $\eta$  ensure good agreement between EAM- and DFT-calculated cohesive energies, bulk modulus, and size-dependent cluster energies. The numerator part of the pairwise interaction  $\phi(R_{ij})$  in Eq. (3) is a generalized two-body Morse potential combining short-range repulsive exponential and long-range attractive exponential.  $r_e$  is the nearest-neighbor distance and  $A, B, \alpha, \beta$  are adjustable parameters. The denominator in Eq. (3) is a cutoff term so that  $\phi(R_{ij})$  approaches zero as  $R_{ij}$  increases from the cutoff range. The cutoffs for the repulsive and attractive interactions are determined by parameters  $\kappa$  and  $\lambda$ , respectively. Downhill simplex method is used for the optimization of adjustable parameters in the functionals.<sup>31</sup> The target function for optimization is the norm of residual between DFT and EAM energies across a set of geometries that includes bulk, surface slabs, and clusters.

For Pd-Au crosspair potential, we have used the same functional form as Eq. (3) but reparameterized it to fit PdAu alloy properties. We found that such a scheme yields same or better results than considering a weighted average of two-body pairwise interaction of respective metals.<sup>16,30</sup> Furthermore, since the value of  $f_e$  has no effect on any of the el-

emental property of metals, we fine tuned the ratio of  $f_e$  between Pd and Au to achieve best agreement with the alloy DFT data.<sup>32</sup>

### C. Monte Carlo simulations

In order to probe the segregation properties of PdAu nanoparticles of different sizes, and composition at different temperatures, we have carried out Monte Carlo simulations by initially creating a random distribution of palladium and gold atoms throughout the nanoparticle. The lattice constant for the alloy is estimated from Vegard's law and kept fixed in the simulation. A particular atom is then selected at random and exchanged with another randomly chosen atom of different type. The energy of nanoparticle before and after the exchange is then calculated using the parameterized EAM potentials. If the resulting change in total energy ( $\Delta E$ ) is negative, the configuration is accepted. However, if the change in total energy is positive, the configuration is accepted only if  $\exp(-\Delta E/kT)$  is greater than a random number selected from a uniform distribution.<sup>33</sup> This procedure is repeated for over million steps for each of the cases we studied. At finite temperatures, the final morphology of the particle is obtained by taking a statistical average of the MC snapshots in the last 10 000 steps, where it has already reached equilibrium. The simulations are run for truncated-octahedron PdAu alloy nanoparticles with different composition ratios (Pd<sub>0.9</sub>Au<sub>0.1</sub>, Pd<sub>0.75</sub>Au<sub>0.25</sub>, Pd<sub>0.5</sub>Au<sub>0.5</sub>, Pd<sub>0.25</sub>Au<sub>0.75</sub>, Pd<sub>0.1</sub>Au<sub>0.9</sub>) and different particle sizes (55, 147, 561, 2057, 5083 atoms) under different temperatures ( $T=273, 523, 773, 1023, \text{ and } 1273 \text{ K}$ ). We analyzed the concentration

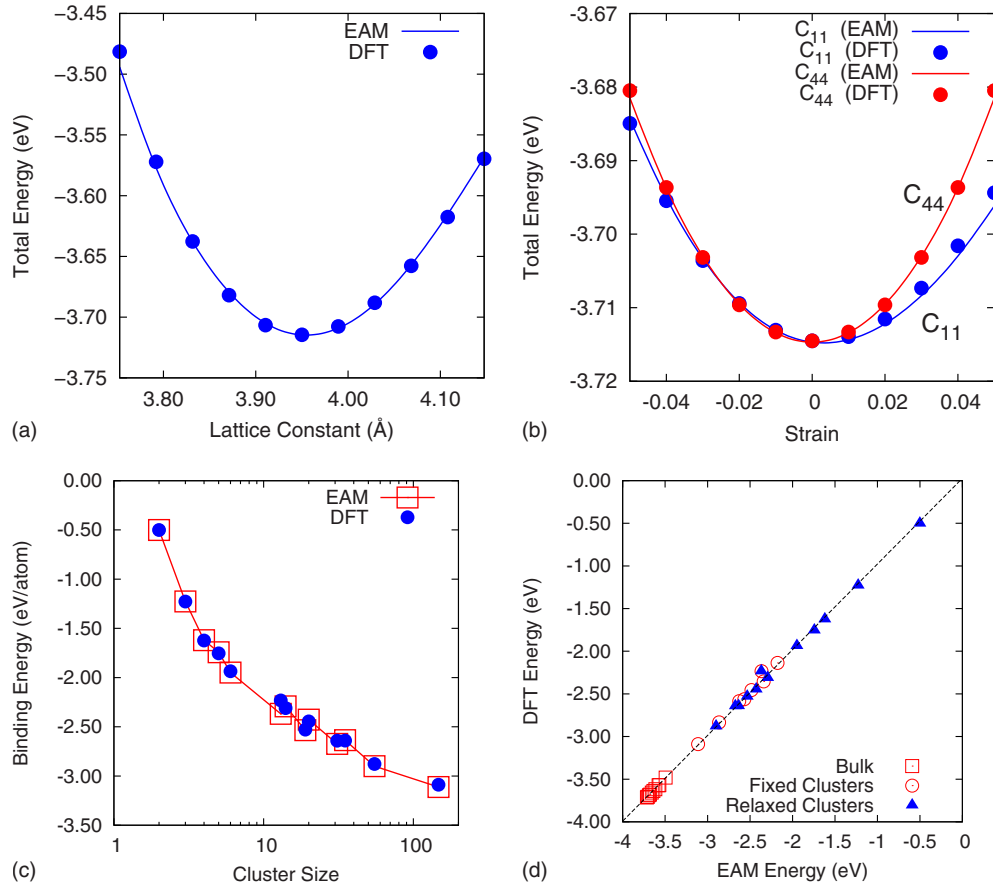


FIG. 4. (Color online) Comparison between DFT and EAM energies for Pd bulk and Pd nanoparticles. (a) Total energy for bulk Pd as a function of lattice constant. (b) Total energy for bulk Pd as function of strain (elastic constant  $C_{11}$  and  $C_{44}$ ). (c) Binding energy per atom as a function of Pd cluster size. (d) Correlation between EAM energies and DFT energies for Pd bulk and clusters.

and morphology of the metal distributions in the alloy nanoparticles. It is worth noting that due to the size effect on melting temperature, those small diameter nanoparticles are likely to melt at much lower temperature than the maximum simulation temperature of 1273 K (Ref. 34) and our conclusion only holds for PdAu alloy nanoparticles up to their melting temperature. Based on liquid drop model,<sup>35</sup> our highest simulation temperature of 1273 K is comparable to the melting temperature of the 5083-atom PdAu nanoparticle.

### III. RESULTS AND DISCUSSION

#### A. DFT calculations and EAM parameterization

The parameterized EAM gives accurate results for both the bulk and nanoparticle energies. Figures 4(a) and 4(b) show the comparison between DFT and EAM energies for bulk Pd. The dots in these figures represent DFT data points and the solid curve represents the results from parameterized EAM calculations. It can be seen that the EAM potential faithfully reproduced all the bulk properties, such as the lattice constant, cohesive energy, and shear distortion. Figure 4(c) shows the average binding energy per atom as the size of the cluster decreases. Conventional EAM scheme fitted to bulk properties alone does not describe the energies of small clusters well.<sup>19</sup> By adding an additional spline in the low

electron-density region and incorporating the cluster energies directly into the fitting procedure, our EAM gives quantitatively accurate results for the energies of nanoparticles. The linear line in Fig. 4(d) with a correlation coefficient ( $R^2$ ) of 0.99 demonstrates the good correlation between EAM and DFT energies for both Pd in bulk and cluster environment. The parameterized EAM potential hence, predicts accurately not only energies of metal clusters with interatomic distances fixed at bulk lattice constant [“fixed clusters” in Fig. 4(d)], but also energies of relaxed clusters [“relaxed clusters” in Fig. 4(d)]. We have followed the same protocol in fitting the EAM potential for Au. In both cases,  $R^2$  between DFT data and EAM is larger than 0.98, indicating excellent correlation and good quality of the EAM potential for both metals. The parameters for pure Pd and Au are tabulated in Table I and the corresponding electron density ( $\rho$ ), embedding function ( $F$ ), and pairwise interaction ( $\phi$ ) are plotted in Figs. 5(a)–5(c), respectively.

The segregation of one particular metal to the surface is not uncommon in alloy nanoparticles and it can have profound impact on catalysis since surface atoms are primarily responsible for catalytic reactions. Au, being a noble metal, has smaller surface energy than Pd, and is expected to segregate to the surface so that total energy of the system is minimized. The negative heat of formation of PdAu alloy act as a compensating factor and tends to promote PdAu mixing

TABLE I. EAM parameters for Pd, Au, and PdAu alloy.

Param	Pd	Au	Pd-Au	Param	Pd	Au	Param	Pd	Au
$r_e$	2.7931	2.9557	2.5056	$F_{n0}$	-2.2575	-2.0977	$F_{ne}$	-2.2947	-2.1394
$f_e$	1.4928	1.1500		$F_{n1}$	-0.5163	-0.4809	$\Gamma$	4.6543	4.6534
$\rho_e$	19.9664	15.3629		$F_{n2}$	1.1767	-2.5861	$\Psi$	0.7584	0.7540
$\alpha$	8.6052	8.1432	9.9702	$F_{n3}$	0.2276	-0.1795	$\rho_m$	0.3127	0.8082
$\beta$	4.6543	4.6534	4.4216	$F_0$	-2.2986	-2.1396	$F_{m0}$	-1.5185	-2.0803
$A$	0.3945	0.2463	0.3769	$F_1$	-0.0000	-0.0000	$F_{m1}$	-0.6368	-0.2169
$B$	0.5707	0.3505	0.5852	$F_2$	1.4335	1.8111	$F_{m2}$	3.5613	1.8561
$\kappa$	0.5962	0.4267	0.4469	$F_3$	-2.6267	-0.3335	$F_{m3}$	2.6796	-0.0072
$\lambda$	0.7584	0.7540	0.8769	$\eta$	0.8943	1.2930			

rather than having them completely phase separate. The final morphology of the PdAu nanoparticle is therefore, a balance of these two competing mechanisms. It is worth noting that energetics of segregation to edge and vertex sites on nanoparticles can be quite different from segregation to a flat surface.

Figure 5(d) depicts alloy heat of formation for 1:3, 3:1, and 1:1 PdAu alloy as a function of lattice constant. DFT calculations correctly predict the negative heat of formation for PdAu alloy as evidenced by the negative heat of formation at equilibrium lattice distances. The parameterized EAM

alloy potential is also reasonably accurate for predicting the alloy heat of formation. To accurately describe the segregation of metal to the flat surface, DFT energies of the 33 distinctive PdAu slabs with different segregation configurations were calculated (a subset is depicted in Fig. 1). Each connected line segment on Fig. 5(e) represents all the possible configurations for a fixed PdAu stoichiometry. Within each line segment, the configuration is ordered by the number of Au atoms on the surface in ascending order. From this set of data, it can be seen that Au segregation to the surface is energetically most favorable. The solid squares, which rep-

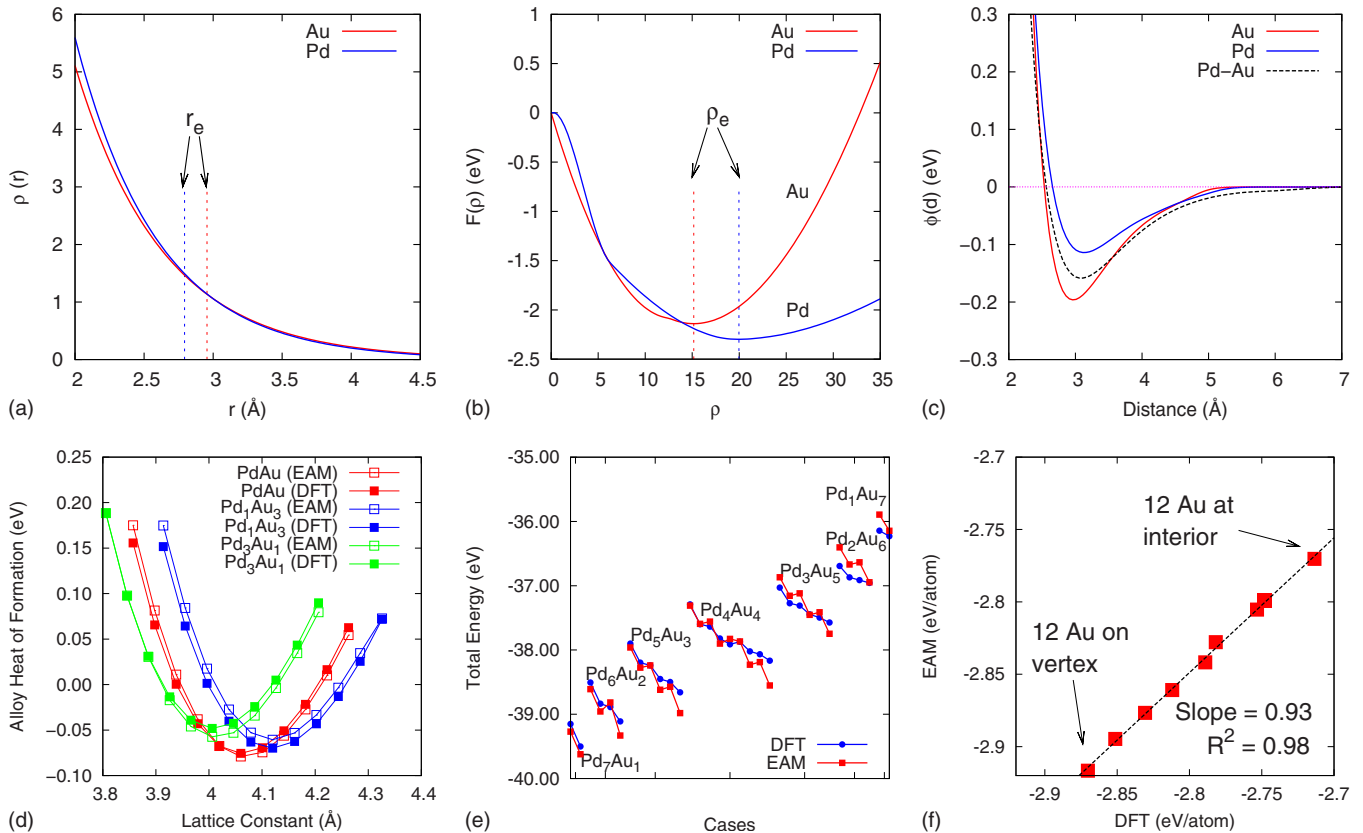


FIG. 5. (Color online) (a) Electron density  $\rho(r)$  for Au and Pd. (b) Embedding functional  $F(\rho)$  for Au and Pd. (c) Pairwise interaction  $\phi$  and crosspair potential for Au and Pd. (d) The alloy heat of formation for PdAu alloy in 1:3, 2:2, and 3:1 composition ratio. (e) DFT and EAM energies for PdAu slabs with different segregation configurations. (f) Correlation between DFT and EAM for Pd<sub>43</sub>Au<sub>12</sub> nanoparticles with different segregation configurations.

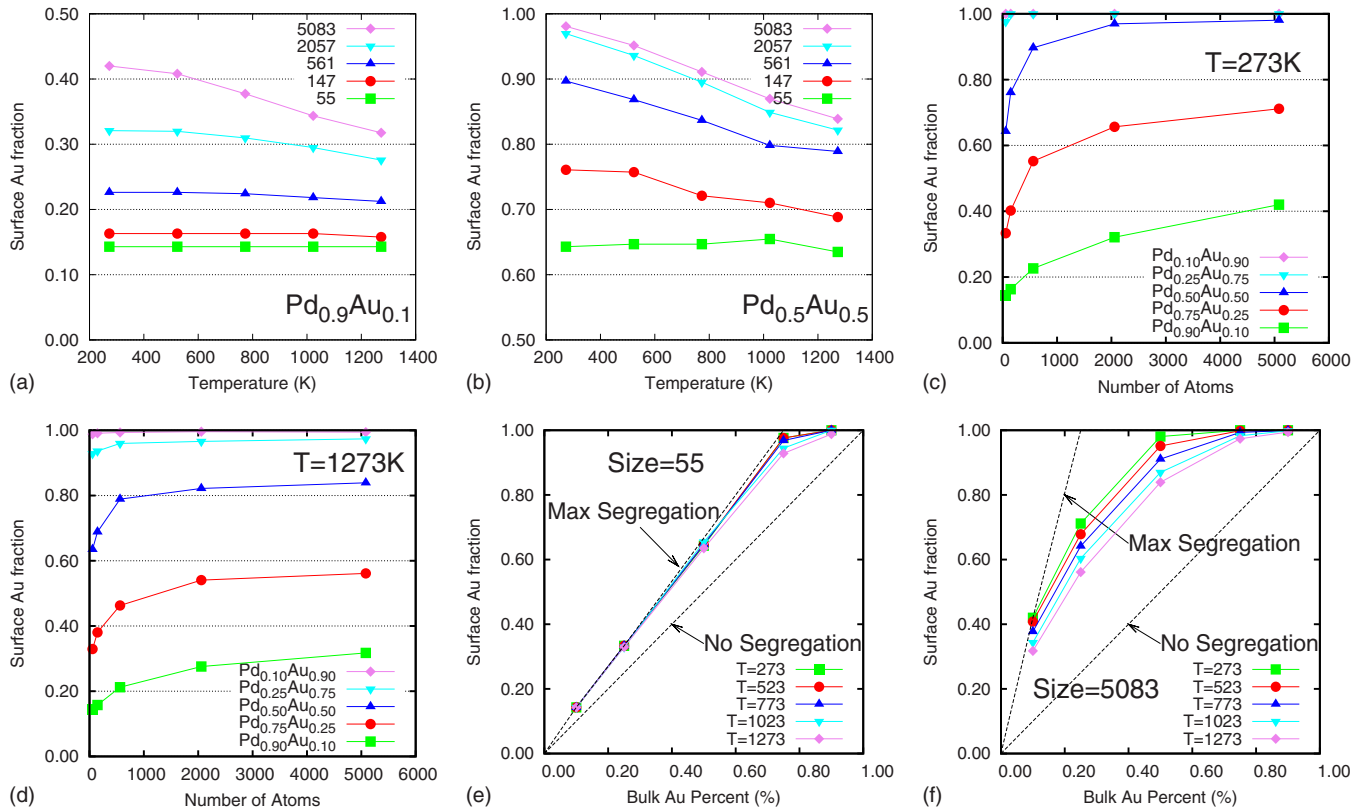


FIG. 6. (Color online) Segregation of PdAu nanoparticles: (a) Pd rich and (b) 1:1 ratio PdAu nanoparticle under different temperatures. Different sized PdAu nanoparticle at (c) 273 and (d) 1273 K. PdAu nanoparticle as a function of concentration for (e) a 55-atom NP and (f) 5083-atom NP.

resent EAM calculations, closely follow the DFT data points (solid circles) and confirm validity of EAM values.

To further validate the robustness of the cross-pair potential, we compared the energies of a 55-atom  $\text{Pd}_{43}\text{Au}_{12}$  nanoparticles with different segregation profiles (Fig. 3). The bottom left point on Fig. 5(f) corresponds to the  $\text{Pd}_{43}\text{Au}_{12}$  particle, where all the 12 Au atoms are segregated to the surface, while the top right point represents the case where all the 12 Au atoms are encapsulated within the nanoparticle. The intermediate points represents the configurations with partial Au segregation to the surface. Even though the slope for the correlation in Fig. 5(f) slightly deviates from unity since the synergetic alloying effect is not accurately captured by EAM, the energy ordering between particles with different segregation profiles is still in exact agreement with the DFT result. Thus the parameterized EAM potential is capable of describing the metal segregation in nanoparticles with reasonable accuracy.

### B. MC simulation of PdAu nanoparticles

The Pd-Au EAM potential described in previous section has been shown to give accurate results for segregation to surfaces, edge, and vertex. Herein, we employed the EAM potential to carry out Monte Carlo simulations to study how different factors such as temperature, particle size, and composition ratios would change the surface concentration of respective metals in PdAu alloy nanoparticles.

Figures 6(a) and 6(b) compare the segregation in PdAu nanoparticles with different composition ratios. Figure 6(a) represents a Pd-rich nanoparticle ( $\text{Pd}_{0.9}\text{Au}_{0.1}$ ) while Fig. 6(b) represents a PdAu alloy nanoparticle with 1:1 composition ratio. Layer by layer oscillation in concentration has been observed, where the outmost nanoparticle layer is Au rich while the sublayer is Pd rich.<sup>26</sup> This layering effect is consistent with the lower surface energy of Au and the negative PdAu heat of formation as shown in Fig. 5(d). For the current study, we focus on the surface layer since it is most relevant to active sites in catalysis. It can be seen that the surface concentration of Au is significantly enriched as compared to its bulk composition ratio in both cases. The surface composition of small particles is especially resistant against temperature effect. This is primarily due to the fact that small nanoparticles are dominated by vertex and edge atoms, where Au and Pd atoms have larger energy differences at those site. From Fig. 5(e), we can estimate the Au segregation energy to surface to be around 0.35 eV from the energy difference between two configurations of  $\text{Pd}_7\text{Au}_1$ . However, the estimated Au segregation energy to vertex site from the energy difference between configurations of 12 Au on vertex and 12 Au at interior [Fig. 5(f)] is around 0.72 eV. Due to this larger energy difference, even the highest temperature we studied (1273 K) is not enough to invert the surface Au concentration. Thus it can be concluded that small PdAu clusters would remain Au segregated under temperature below their melting point. For larger nanoparticles, on the con-

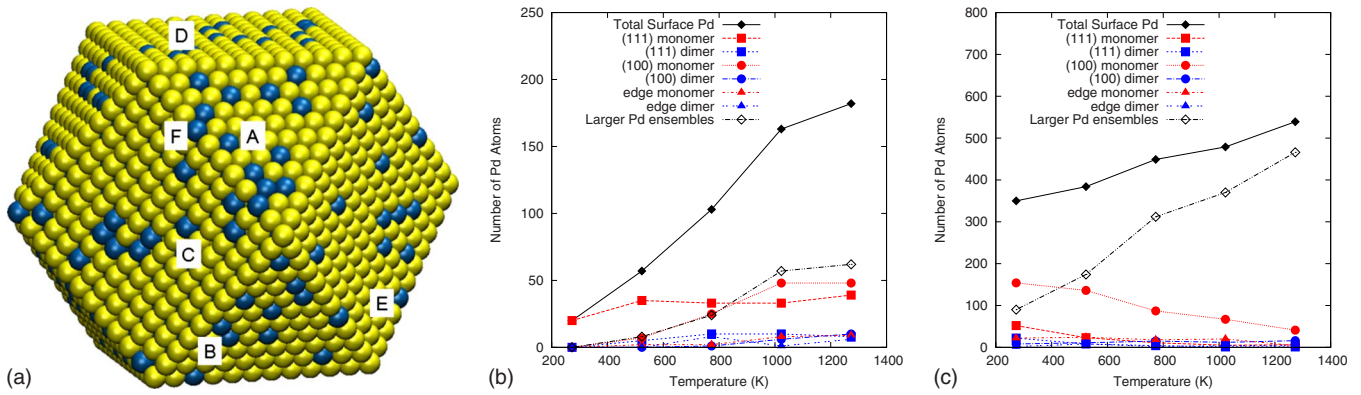


FIG. 7. (Color online) (a) Snapshot of 5083-atom PdAu NP at 1023 K. Labels in the schematic represent different types of monomers and dimers. A represents (111) monomer, B represents (111) dimer, C represents (100) monomer, D represents (100) dimer, E represents edge or vertex monomer, and F represents edge or vertex dimer. (b) Statistics for Pd monomer and dimer distribution on PdAu 5083-atom NP. (c) Statistics for Pd monomer and dimer distribution on Pd<sub>3</sub>Au<sub>1</sub> 5083-atom NP.

trary, we do see a significant decrease in surface Au concentration at higher temperatures.

The surface Pd concentration enrichment with respect to temperature is most significant for PdAu alloys with Au concentration in the 25–50 % ratio. High Au concentration leads to a Au-passivated surface irrespective of the temperature, while in low Au concentration alloys, the surface concentration change is limited by the amount of Au available. Figures 6(c) and 6(d) show the segregation versus particle size at  $T = 273$  and  $1273$  K, respectively. For Au-rich nanoparticles, the surface forms monolayer of Au. In the Pd-rich particles, we see an initial sharp increase in the Au concentration followed by an asymptotic plateau. Since the maximum number of surface Au atoms cannot exceed total number of Au atoms in the alloy, which is applicable to Pd-rich alloys, we can expect the surface Au concentration to follow a  $N^{1/3}$  curve with respect to the total number of atoms. This analysis quantitatively agrees with the results for Pd-rich nanoparticles in the lower portion of Figs. 6(c) and 6(d).

Figures 6(e) and 6(f) show the segregation behavior of nanoparticles (from a 55-atom nanoparticle to a 5083-atom nanoparticle) with different alloy composition ratios. The diagonal line across the graph indicates no segregation scenario while the other dotted line shows the maximum possible degree of segregation as permitted by the number of available Au atoms in the particle. It is clear from both these plots that for small nanoparticles, the Au atoms fully segregate to the surface until it reaches a full monolayer. The degree of segregation is less pronounced in large nanoparticles, where the negative heat of formation of PdAu keeps a fraction of Au intermixed in the nanoparticle to maintain its energetically favorable equilibrium structure. An entropic effect can be seen for 5083-atom NP where the concentration of Au on the surface continually decreases as a function of temperature.

Our statistics on the distribution of Pd monomers and dimers on the 5083-atom PdAu nanoparticle surface show that even though entropic effect has been seen for both PdAu alloys with 1:1 or 3:1 ratio, the change in Pd monomers and dimers distributions is quite different. Figure 7(a) labels different types of monomers and dimers on the nanoparticle

surface and their distribution is plotted as a function of temperature for PdAu and Pd<sub>3</sub>Au<sub>1</sub> composition in Figs. 7(b) and 7(c). As can be seen from the graph for PdAu 5083-atom NP, the total Pd atom concentration increase on the surface with increasing temperature is primarily due to the increase of (100) monomers and large Pd ensembles (islands containing three Pd atoms or more), while the number of (111) monomer remains roughly constant. In the case of Pd<sub>3</sub>Au<sub>1</sub> NP, however, the concentrations of both monomers and dimers decrease with temperature. This decrease is because of the high concentration of Pd within the particle. Significant amount of Pd atoms are present on the surface even at low temperatures and more Pd segregation to the surface at elevated temperatures leads to the formation of large Pd ensembles. In both nanoparticles, vertex and edge sites are primarily dominated by Au atoms. Recently, it has been shown that Pd monomer or dimers are critical ensembles for enhanced reactivities.<sup>4,5</sup> With a good understanding of reactivity of these different ensembles on the surface, our EAM potential and MC simulation will prove to be a useful tool in designing alloy nanoparticles with better reactivity.

#### IV. CONCLUSIONS

We have developed and parameterized an accurate EAM potential for the modeling of PdAu alloy nanoparticles. The potential yields accurate results for both the bulk properties and nanoparticle energies. We have used the EAM potential in studying the segregation behavior of PdAu nanoparticles with different sizes and composition ratios under different temperatures. Our MC simulation indicates an almost full segregation of Au to the surface in small nanoparticles. In large nanoparticles, the statistical distribution of Pd monomers and dimers depends on both temperature and composition ratios. The influence of different factors have been presented and discussed to give insight into PdAu nanoparticle segregation.

#### ACKNOWLEDGMENTS

We thank M. I. Baskes and M. Neurock for helpful discussions.

\*bshan@nanostellar.com

†kjcho@utdallas.edu

- <sup>1</sup>M. Watanabe and S. Motoo, *J. Electroanal. Chem. Interfacial Electrochem.* **60**, 275 (1975).
- <sup>2</sup>W. F. Lin, M. S. Zei, M. Eiswirth, G. Ertl, T. Iwasita, and W. Vielstich, *J. Phys. Chem. B* **103**, 6968 (1999).
- <sup>3</sup>P. Liu and J. Norskov, *Phys. Chem. Chem. Phys.* **3**, 3814 (2001).
- <sup>4</sup>F. Maroun, F. Ozanam, O. Magnussen, and R. Behm, *Science* **293**, 1811 (2001).
- <sup>5</sup>M. Chen, D. Kumar, C. Yi, and D. Goodman, *Science* **310**, 291 (2005).
- <sup>6</sup>B. Pawelec, A. Venezia, V. L. Parola, E. Cano-Serrano, J. Campos-Martin, and J. Fierro, *Appl. Surf. Sci.* **242**, 380 (2005).
- <sup>7</sup>L. Guzzi, A. Beck, A. Horvath, Z. Koppány, G. Stefler, K. Frey, I. Sajo, O. Geszti, D. Bazin, and J. Lynch, *J. Mol. Catal. A: Chem.* **204-205**, 545 (2003).
- <sup>8</sup>J. Rodriguez, *Surf. Sci. Rep.* **24**, 223 (1996).
- <sup>9</sup>D. Yuan, X. Gong, and R. Wu, *Phys. Rev. B* **75**, 085428 (2007).
- <sup>10</sup>D. Yuan, X. Gong, and R. Wu, *Phys. Rev. B* **78**, 035441 (2008).
- <sup>11</sup>G. Mazzone, I. Rivalta, N. Russo, and E. Sicilia, *J. Phys. Chem. C* **112**, 6073 (2008).
- <sup>12</sup>W. Kohn, *Rev. Mod. Phys.* **71**, 1253 (1999).
- <sup>13</sup>M. S. Daw and M. I. Baskes, *Phys. Rev. B* **29**, 6443 (1984).
- <sup>14</sup>S. M. Foiles and M. S. Daw, *Phys. Rev. B* **38**, 12643 (1988).
- <sup>15</sup>A. P. Sutton and J. Chen, *Philos. Mag. Lett.* **61**, 139 (1990).
- <sup>16</sup>R. A. Johnson, *Phys. Rev. B* **39**, 12554 (1989).
- <sup>17</sup>D. W. Brenner, *Phys. Rev. B* **42**, 9458 (1990).
- <sup>18</sup>S. M. Foiles, M. I. Baskes, and M. S. Daw, *Phys. Rev. B* **33**, 7983 (1986).
- <sup>19</sup>B. Lee and K. Cho, *Surf. Sci.* **600**, 1982 (2006).
- <sup>20</sup>J. P. Perdew, K. Burke, and M. Ernzerhof, *Phys. Rev. Lett.* **77**, 3865 (1996).
- <sup>21</sup>G. Kresse and J. Furthmüller, *Comput. Mater. Sci.* **6**, 15 (1996).
- <sup>22</sup>C. Kittel, *Introduction to Solid State Physics* (Wiley, New York, 1996).
- <sup>23</sup>K. Chen, L. R. Zhao, and J. S. Tse, *J. Appl. Phys.* **93**, 2414 (2003).
- <sup>24</sup>H. N. G. Wadley, A. X. Zhou, R. A. Johnson, and M. Neurock, *Prog. Mater. Sci.* **46**, 329 (2001).
- <sup>25</sup>X. Zhou, H. Wadley, R. Johnson, D. Larson, N. Tabat, A. Cerizzo, A. Petford-Long, G. Smith, P. Clifton, R. Martens, and T. F. Kelly, *Acta Mater.* **49**, 4005 (2001).
- <sup>26</sup>H. Deng, W. Hu, X. Shu, L. Zhao, and B. Zhang, *Surf. Sci.* **517**, 177 (2002).
- <sup>27</sup>Z. Bangwei, E. Taglauer, S. Xiaolin, H. Wangyu, and D. Huiqiu, *Phys. Status Solidi A* **202**, 2686 (2005).
- <sup>28</sup>J. Cai and Y. Y. Ye, *Phys. Rev. B* **54**, 8398 (1996).
- <sup>29</sup>X. W. Zhou, R. A. Johnson, and H. N. G. Wadley, *Phys. Rev. B* **69**, 144113 (2004).
- <sup>30</sup>H. R. Gong, L. T. Kong, W. S. Lai, and B. X. Liu, *Phys. Rev. B* **66**, 104204 (2002).
- <sup>31</sup>J. Nelder and R. Mead, *Comput. J.* **7**, 308 (1965).
- <sup>32</sup>X. W. Zhou, H. N. G. Wadley, J.-S. Filhol, and M. N. Neurock, *Phys. Rev. B* **69**, 035402 (2004).
- <sup>33</sup>N. Metropolis, A. W. Rosenbluth, M. N. Rosenbluth, A. H. Teller, and E. Teller, *J. Chem. Phys.* **21**, 1087 (1953).
- <sup>34</sup>P. Buffat and J.-P. Borel, *Phys. Rev. A* **13**, 2287 (1976).
- <sup>35</sup>K. K. Nanda, S. N. Sahu, and S. N. Behera, *Phys. Rev. A* **66**, 013208 (2002).